

Two dimensional silicon nanowalls for lithium ion batteries†

Cite this: DOI: 10.1039/c3ta13546b

Received 5th September 2013
Accepted 11th October 2013

DOI: 10.1039/c3ta13546b

www.rsc.org/MaterialsA

Jiayu Wan,^{‡a} Alex F. Kaplan,^{‡b} Jia Zheng,^{‡c} Xiaogang Han,^a Yuchen Chen,^a Nicholas J. Weadock,^a Nicholas Faenza,^a Steven Lacey,^a Teng Li,^{*c} Jay Guo^{*b} and Liangbing Hu^{*a}

One-dimensional (1-D) nanostructures such as nanowires and nanotubes have been widely explored for anodes with high specific capacity in Li-ion batteries, which effectively release the mechanical stress to avoid structure pulverization. However, 1-D nanostructures typically have a high surface area, which leads to a large irreversible capacity in the first cycle due to a solid electrolyte interface (SEI) formation. Two dimensional (2-D) nanowalls can address the same challenges as 1-D nanostructures, with a much lower surface area. For the first time, we demonstrated a 2-D nanowall structure with silicon for Li-ion batteries. Excellent performance for the first Coulombic efficiency (CE) has been achieved. Such a 2-D nanowall structure can also be applied in other devices with improved performance where nanostructures are needed but a high surface area is problematic.

Introduction

Lithium (Li) ion batteries are one of the most important electrochemical energy storage devices and are widely used in portable electronics. For future Li ion battery powered electronic vehicles, however, electrode materials with higher energy/power density and longer cycle life are needed.^{1–6} Silicon (Si), as a Li ion battery anode material, has a theoretical specific capacity of 4200 mA h g⁻¹, 10 times higher than the conventional graphite anodes used in commercial batteries. Additionally, Si is an earth abundant and environmentally friendly material with a mature manufacturing process in solar cell and semiconductor industries that could

enable mass production for batteries. Enthusiasm aside, there are significant challenges to use Si as an anode for Li ion batteries.⁷ A large volume expansion (up to 400%) and contraction during lithiation and delithiation could result in pulverization of the Si anode. The cracked Si loses contact with the current collector, reducing the accessible capacity over time. The significant volume change also affects the stability of the solid electrolyte interphase (SEI). Recently successful demonstration of using Si nanowires as anodes in Li ion batteries to mitigate pulverization and enhance the cycle life⁷ has led to a surge of interest in developing high performance Si nanostructures and Si nanocomposite anodes for Li ion batteries, including Si–C nanocomposites,^{8–12} Si nanotubes,^{13,14} interconnected nanonets^{15,16} and three dimensional (3-D) Si nanoparticles¹⁷. In order to understand the mechanism of Si as an anode material, fundamental studies on its electrochemical,^{18,19} nanomechanics,^{20–22} and kinetics²² have been reported. The problem of a low first Coulombic Efficiency (CE), however, still exists in the reported nanostructures.

The highly irreversible capacity of the first cycle in any nanostructured electrodes is largely attributed to side reactions and SEI formation, which are directly correlated with the high surface area of nanostructures.^{7,23} This is a fundamental challenge of using nanostructures for electrochemical storage applications. On one side, nanostructured materials such as nanowires and nanoparticles can readily release the mechanical strain during charging, which reduce the potential for pulverization during the first cycle. On the other side, the large surface area of these nanostructures results in a greater amount of side reactions, which occur at the anode–electrolyte interface. The formation of the SEI layer consumes Li ions, contributing to an irreversible consumption of Li. The reduction of surface oxide layers on Si, which are formed when exposing Si anode in air during sample preparation, also leads to irreversible consumption of Li.²⁰ Thus, the large surface area of existing nanostructures plays a major role in the low first CE of those nanostructured Si anodes.

^aDepartment of Materials Science and Engineering, University of Maryland, College Park, MD, 20742, USA. E-mail: Binghu@umd.edu

^bDepartment of Electrical Engineering and Computer Science, University of Michigan, Ann Arbor, MI, 48109, USA. E-mail: Guo@umich.edu

^cDepartment of Mechanical Engineering, University of Maryland, College Park, MD, 20742, USA. E-mail: LiT@umd.edu

† Electronic supplementary information (ESI) available. See DOI: 10.1039/c3ta13546b

‡ These authors contribute equally to this work.

We propose a two-dimensional (2-D) nanowall structure that can effectively address the issues associated with lower dimensional Si nanostructures. Such 2-D nanostructures are fundamentally better for Li-ion batteries, which have not been explored before. A schematic image of the nanowalls is shown in Fig. 1h. Each nanowall possesses a sub-micron scale length and height, and can be as thin as 50 nanometers. The nanowall structure maintains the advantages of other one dimensional (1-D) nanostructures: accommodates large volume expansion without pulverization, obtains direct electrical contact with the current collector for fast electron transport, and maintains a short Li insertion distance. Most importantly, the nanowall structure has approximately 50% less specific surface area than nanowires of similar height and width. Thus, the first CE is expected to be higher for the 2-D nanowall structure than for 1-D nanostructured anodes in Li-ion batteries. Currently, there are a few reports^{15,24–28} that discuss 2-D electrodes including “nanowalls” for Li ion batteries, which also provide alternative methods²⁹ for nanowall fabrication. However, the reported nanowalls show an inter-connected structure that is easy to pulverize during volume cycling, thus achieving a low first CE.

Here, for the first time we designed a periodic, amorphous Si (a-Si) nanowall structure *via* nanoimprint lithography (NIL)³⁰ and investigated its electrochemical and mechanical properties as an anode in Li ion batteries. We demonstrate a high CE for the first cycle due to the low specific surface area of the nanowall electrode. Cycling results show that our Si nanowall anodes created by NIL achieve a high first CE (83.4%), high stability (40 cycles) and a good rate performance (1000 mA h g⁻¹ at 2 C rate). The electrochemical properties, including the first CE, can be further improved by optimizing the Si nanowall anode including its dimensions, surface impurity and large area uniformity. Si nanowalls are expected to have excellent mechanical flexibility and are suitable for flexible energy storage for portable electronics, flexible displays, *etc.*^{31–33} Similar concepts can be applied to other devices^{34–36} such as solar cells, where nanostructures are needed for light-trapping and a low surface area is required to avoid surface recombination.

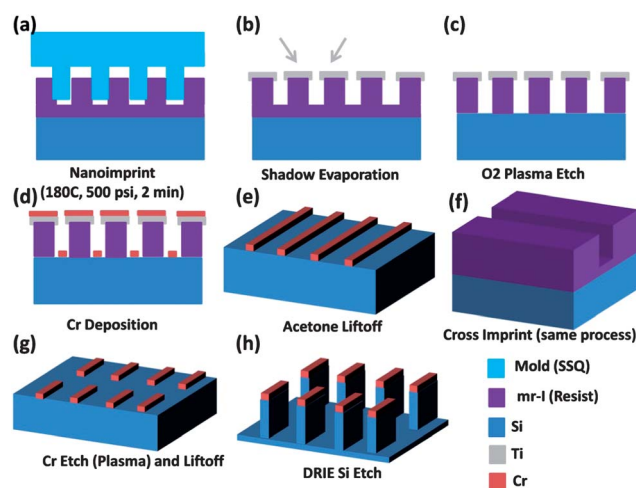


Fig. 1 Outline of the NIL process for Si nanowall anode on an SS substrate (the SS substrate is not shown in this figure).

Experimental section

Si nanowall fabrication

Si nanowalls are fabricated in two steps. First, a highly pure Cr (film thickness 20 nm, ESPI metals)/a-Si (film thickness 900 nm, Materion corporation, 99.999%) is deposited by electron-beam deposition (Temescal BJD-1800). The layer of Cr is used to enhance the binding of the a-Si to the substrate. Energy dispersive X-ray spectroscopy (EDS) results show that the purity of a-Si is 97% (Fig. S5†). Second, the nanoimprint patterning process (Fig. 1) begins by spinning the imprint resist (mr-I 8030, Microchem). The resist is spun onto the sample and imprinted with a 220 nm period silsesquioxane (SSQ) mold³⁶ in a NX2000 Nanoimprinter (Nanonex, NJ) (Fig. 1a). Directional evaporation of Ti onto the resist is used to increase the effective linewidth of the resist structure, decreasing the width of the opening down to approximately 50 nm, which is the desired width of the walls (Fig. 1b). After reactive ion etching (RIE) with oxygen plasma to remove the residual resist (Fig. 1c), Cr is deposited and a lift off process is performed to generate a 220 nm Cr grating with a 50 nm linewidth (Fig. 1d). In order to create a disconnected wall structure, a subsequent imprint is then performed with a 700 nm period mold perpendicular to the 220 nm period Cr grating (Fig. 1e). After the residual layer of the resist is removed, RIE is again used to remove the Cr grating in the portion of area exposed by the 700 nm resist pattern (approximately 100 nm in width) (Fig. 1f). The final Cr pattern is then used as a mask for DRIE to create the nanowalls (Fig. 1g).

Li ion battery fabrication and testing

Coin cells are made of Si nanowalls as the working electrode, a polymer separator, lithium metal foil as the counter electrode and 1.0 M LiPF₆ in 1:1 w/w ethylene carbonate/diethyl carbonate (Novolyte technologies). CR2032 half cells were assembled inside an Ar-filled glove box and tested using a Biologic VMP3 multichannel system. Si nanowall half cells were cycled between 1.0 V and 0.01 V.

Material characterization

Si thin film and Si nanowalls were characterized with a Hitachi SU-70 analytical scanning electron microscope with an energy-dispersive X-ray detector (Bruker's silicon drift detector). After cycling, coin cells were disassembled inside a glove box, and nanowall electrodes were washed with acetonitrile and 0.1 M H₂SO₄ to remove the residual electrolyte, lithium salts and the SEI layer. Samples were dried at room temperature before SEM examination.

Results and discussion

Fabrication and characterization of Si nanowalls

NIL can be used to generate high-resolution feature sizes on a scale of tens of nanometers over large areas. Recently, structures have been fabricated for applications in fields such as photonics,^{37,38} transparent metal electrodes,³⁹ solar cells,⁴⁰ and sensors,⁴¹ to name a few. To fabricate the nanowall structure, a

typical thermal imprint process begins by placing a pre-patterned mold directly in contact with a resist-coated substrate. High temperature and pressure are then applied to reflow the resist into the mold, creating a mirror image of the pre-patterned features in the resist. Using these features to create a mask, we can then transfer nano-scale patterns into Si and create high aspect-ratio Si nanostructures with depths in the micron range. This is done with deep reactive ion etching (DRIE), specifically utilizing a cycled “Bosch” process, which has been used in the past to create nanostructures with aspect ratios greater than 50 : 1.⁴² The NIL process is illustrated in Fig. 1.

As shown in Fig. 1 each Si nanowall is 900 nm high, 600 nm long and 50 nm thick. Perpendicular to the wall surface, the structure has a 220 nm period, with a space of 170 nm between each wall. Lengthwise, the periodicity is 700 nm with 100 nm spacing between walls. A discontinuous nanowall pattern rather than a continuous grating is proposed here to allow each nanowall to “breathe”, relaxing the stress resulting from lithiation/delithiation induced volume expansion/contraction.

We characterized the morphology and composition of the prepared Si nanowall structure with a scanning electron microscope (SEM) equipped with a Bruker EDS detector. The highly uniform size and lateral distribution of the Si nanowall array is shown in Fig. 2a. In Fig. 2b (top view), the length and thickness of the nanowalls are measured to be about 600 nm and 50 nm, respectively. The space in between the nanowalls is designed to accommodate volume expansion during charge-discharge. Fig. 2c shows the EDS mapping image of the Si nanowalls. From Fig. 2b and c we observed some edge roughness associate with nanowalls. This edge roughness is generated during fabrication due to the roughness of the shadow evaporation, which masks the Cr deposition. There is also the so-called “scalloping” which occurs during the DRIE Bosch process on the sidewalls of the nanostructure. Fig. 2d shows the

EDS analysis of one prepared Si nanowall sample. We confirmed our composition of the whole electrode with the help of Fig. 2d, showing three elements of Si, Fe and Cr which correspond to nanowalls, the substrate and binding layer (also residual Cr mask), respectively.

The top down nanoimprint technique ensures that Si nanowalls are in direct electronic contact with the current collector, have a suitable specific surface area that allows for fast charge-discharge, while reduce the amount of SEI formation thus contributing to a high first CE. The small thickness of the nanowalls (50 nm in our experiment) allows for a short diffusion path of Li ions, increasing the potential for high power applications. The spacing between the nanowalls on four sides helps avoiding the nanowalls from touching each other during volume expansion, allowing a stable cycling performance of the nanowall electrodes.

Electrochemical properties of Si nanowalls in Li half cell

After fabrication, the samples were dried in a 100 °C vacuum oven overnight and then directly assembled into coin cells in an Ar filled glove box. Electrochemical measurements were performed using a Biologic VMP3 electrochemical workstation; the cycling performance and electrochemical impedance spectroscopy (EIS) results are presented in Fig. 3. Fig. 3a shows the cycling performance and Coulombic efficiency of the Si nanowalls at the rate of 840 mA g⁻¹ for 40 cycles. The first charge and discharge capacity of the Si nanowalls are 2350 mA h g⁻¹ and 1961 mA h g⁻¹, respectively, corresponding to a first CE of 83.4%. This initial CE of the Si nanowall anodes still has room for improvement by optimizing the design and fabrication of nanowalls or surface modification.^{11,43–45} The Si nanowall anode demonstrates stable cycling performance, retaining a discharge capacity of 1801 mA h g⁻¹ after 40 cycles, which is 90% of the

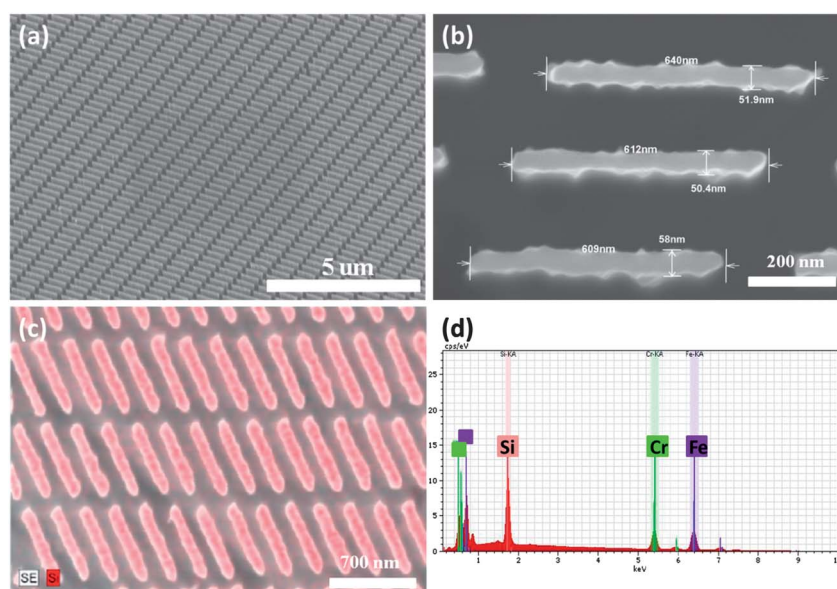


Fig. 2 (a) SEM images of a large area and uniformly distributed Si nanowall structure, (b) SEM image which shows the dimensions of the Si nanowalls, (c) SEM EDS mapping images of Si nanowalls, and (d) energy dispersed X-ray spectroscopy of Si nanowall/substrate, with peaks of Si, Cr and Fe.

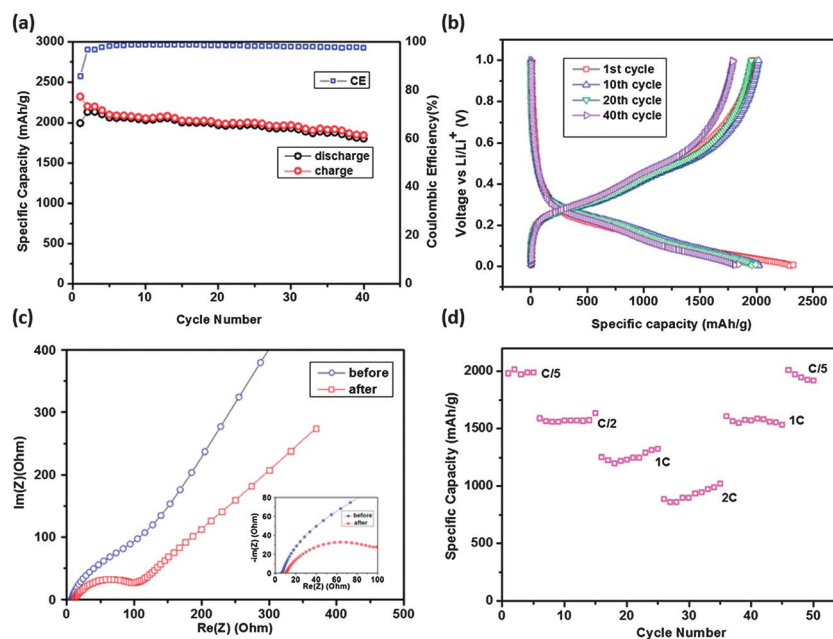


Fig. 3 (a) Electrochemical cycling performance of Si nanowall anodes. (b) Voltage profile of 1st, 10th, 20th and 40th cycle of the Si nanowalls. (c) EIS plot of the battery before cycling (blue) and after 40 cycles (red). (d) The rate performance of the Si nanowall half cell.

initial value. The capacity retention is highlighted in Fig. 3b, which plots the charge and discharge voltage profiles of 1st, 10th, 20th and 40th cycles. The capacity suffers almost no loss during the first twenty cycles. The typical voltage profile of amorphous Si (a-Si) is seen during lithiation of a-Si at approximately 0.49 V vs. Li/Li⁺.¹⁰ Fig. 3c shows the EIS data of the Si nanowall half cells. Both EIS data before and after cycling were taken at the fully delithiated state. The EIS results before cycling and after 40 cycles are shown by the blue and red curves, respectively. Bulk resistance of the cell is equal to the first intersection of the EIS curve with the real impedance axis. From the inset, we observed that the initial high-frequency resistance of 8 ohms (before the cycling test) increases to 10 ohms after 40 cycles, indicating the formation of an SEI layer. The diameter of the semicircle represents the charge transfer resistance (R_{ct}) of the cell. We observed that the charge transfer resistance of the Si nanowall half cell decreases after cycling. Examination of the nanowall structures after cycling in SEM helps to explain this phenomenon (Fig. 4). After 40 cycles, the individual nanowalls have become more porous (Fig. 4b). As the cycling progress, the increasing porosity of the Si exposes more surface area to the electrolyte, increasing the charge transfer process and reducing R_{ct} . This is confirmed by the rate performance data in Fig. 3d.

To determine the rate performance, the half cells were cycled at charge–discharge rates ranging from C/5 to 2 C. Charging at higher rates reduces the capacity of batteries as the Li insertion reaction is limited by diffusion and reaction at the interface. The formation of a porous structure during cycling increased the surface area of the electrode, resulting in an increasing capacity of the high rate cycles. Comparing the capacity of a 1 C battery at cycles 15–25 and 35–45 shows an increase of 200 mA h g⁻¹ for later cycles. The capacity of the battery at 2 C is

about 1000 mA h g⁻¹, 3 times higher than the capacity of conventional graphite electrodes.

The half cells were disassembled in a glove box in the delithiated state, and the residual electrolyte and SEI were washed away to expose the Si nanowalls. The morphology of the electrode was examined by SEM as shown in Fig. 4. From Fig. 4a we see that the Si nanowalls retain their wall structure and remain attached to the substrate, indicating good structural stability and binding. The cracked surface on top of the nanowalls is a residual layer of Cr left over from the nanowall fabrication (Fig. S6†). The cracking and distortion of this layer suggests large volume changes and stress during cycling. The space between each nanowall is largely reduced, indicating a significant volume change of the Si nanowall structure by lithiation. Fig. 4b shows the porous structure of the Si nanowalls after cycling. Both the sides and the top of the nanowalls have become porous. We also observed slight twisting of the nanowalls after 40 cycles in both Fig. 4a and b. Overall, Si nanowalls can withstand significant volume changes associated with lithiation and delithiation. A higher magnification image of the porous structure on the Si sidewall is shown in Fig. 4c. It seems from this image that the porous structure formed many nano-channels in the Si sidewalls, allowing Li⁺ ions to diffuse faster inside. However, during the formation of the porous structure, the active material will detach from the walls, resulting in a slight capacity reduction.

Nanopore formation mechanism by mechanical means

As shown in Fig. 4a and b the nanowall structure thickens and develops a very rough surface morphology after 40 cycles, indicating pore formation at both the surface and the interior of

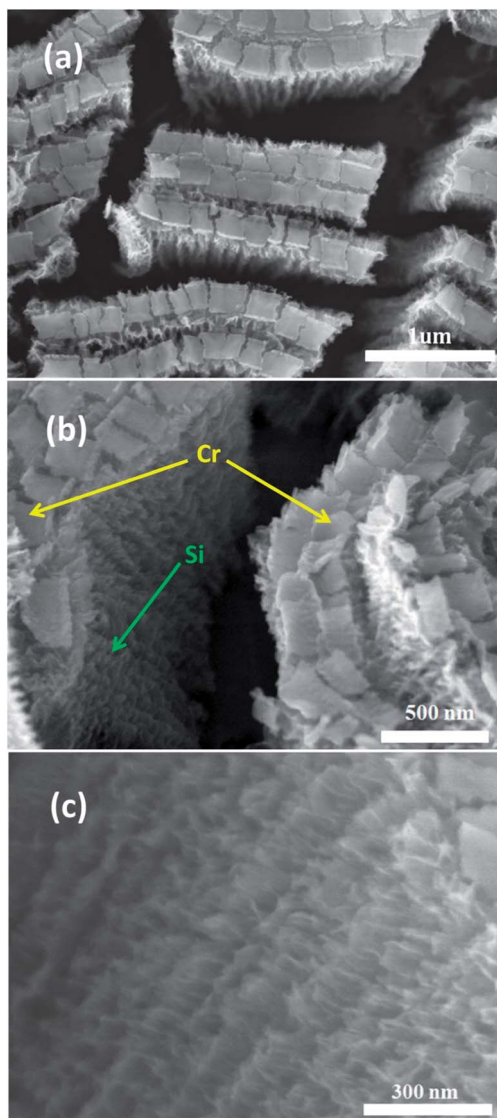


Fig. 4 (a) and (b) SEM images at different magnifications of the Si nanowall anode after cycling. A residual Cr layer from the mask is observed on top of the nanowalls. (c) High magnification SEM image of Si nanowalls after cycling shows the porous structure with an average pore size of ~ 30 nm.

the nanowalls. The formation of such a porous structure is attributed to the hydrostatic tensile stress in the nanowalls induced by lithiation and delithiation, as revealed by the following mechanics modelling. The size of the nanowalls in the modelling is $600 \text{ nm} \times 50 \text{ nm} \times 900 \text{ nm}$ ($L \times W \times D$) for each. During lithiation and delithiation, Li ions insert into and extract from the nanowalls, inducing large cyclic deformation of the Si. As to be shown later, the stress associated with the large deformation in the nanowalls is highly non-uniform (*e.g.*, stress level varies with positions in the nanowalls) and tri-axial. If the Li concentration is sufficiently large, the associated stress can be high enough to cause the plastic flow of the lithiated Si. A cavity in a solid can unstably grow in size by atom diffusion away from the cavity surface driven by sufficiently high hydrostatic stress (defined as the mean stress $\sigma_m = \frac{\sigma_{11} + \sigma_{22} + \sigma_{33}}{3}$).

Therefore, if the lithiation/delithiation-induced mean stress in the Si is high enough, defects in the nanowalls (*e.g.*, voids) could grow unstably, leading to a porous structure. The underlying energetics can be explained by a simple model. The free energy of a lithiated Si with an incipient spherical void of radius R under a mean stress σ_m applied to the void is given by $G(R) = 4\pi R^2 \gamma - \frac{4}{3}\pi R^3 \sigma_m$, where γ is the surface energy of lithiated silicon. Under the lithiation/delithiation-induced stresses, the incipient void tends to grow or shrink to minimize the free energy G , from which one determines a critical void size $R_c = 2\gamma/\sigma_m$. That is, a void with $R < R_c$ shrinks and thus may heal spontaneously while a void with $R > R_c$ unstably grows into a pore of large size. Next, we calculated the lithiation/delithiation-induced stresses in the Si nanowalls, so that the critical void size in different regions of the nanowalls can be estimated, which in turn help decipher the formation of the porous structure after lithiation/delithiation cycles as observed in the experiments.

We simulated the concurrent Li diffusion and mechanical deformation during the initial lithiation and following delithiation of the amorphous Si nanowalls using finite element package ABAQUS 6.10 (see ESI for model details[†]). The extent of lithiation is described by the average Li/Si atomic ratio x_{average} , defined as the ratio of Li atoms in the nanowalls. For example, $x_{\text{average}} = 1$ means that on average one Si atom takes one Li atom in the nanowalls. We assume that the extent of volume expansion has a linear relationship with the lithium content in Li_xSi .⁴⁶ From our experiment, x_{average} reaches 2 at the end of the lithiation cycle, resulting in a 200% volume expansion of the nanowalls (Fig. S1[†]). Simulation results reveal that the mean stress level in the nanowalls increases with the extent of lithiation and nearly saturates as x_{average} approaches 1 (Fig. S4[†]). The distribution of the mean stress at two representative planes of the nanowalls, *i.e.*, the mid-plane ($z = 0$) and the outer surface ($z = h/2$, where h is the nanowall thickness), is shown in Fig. 5b and c, respectively. Here $x_{\text{average}} = 1$. The regions labelled by A through G undergo a significant tensile mean stress ranging from 150 to 600 MPa. As mentioned above, the tensile mean stress state acts as the driving force for the nucleation and growth of nano-pores. For example, during lithiation nano-pore formation is likely to occur in the middle part of nanowalls (regions A, B and E) and near the bottom corners (regions C, D, F and G).

Moreover, simulation results show that during lithiation the area under significant tensile mean stress at the mid-plane of the nanowalls (regions A to D shown in Fig. 5b) is much larger than that at the outer surface (regions E to G shown in Fig. 5c). The mean stress level at the mid-plane is also even higher than that at the outer surface, indicating that the interior of nanowalls is more susceptible to pore formation during lithiation.

In the following delithiation half cycle shown in Fig. 5d and e, the regions experiencing a significant tensile mean stress of 150 MPa to 1 GPa are labelled by a through k. Comparison between the mean stress distributions at the mid-plane and outer surface reveals that, during delithiation, pores are more likely to nucleate and grow near the nanowall outer surface,

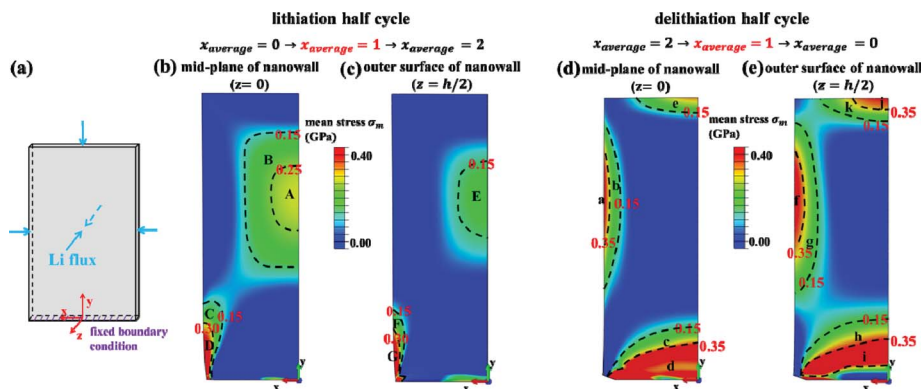


Fig. 5 Lithiation/delithiation-induced mean stresses in the nanowalls. (a) Schematic of the simulation model. The origin of the coordinate system is defined with the origin at the centroid of the bottom surface. (b) and (c) show the mean stress distribution within the mid-plane of the nanowalls ($z = 0$) and the outer surface of the nanowalls ($z = h/2$) during the lithiation half cycle, respectively, with the extent of lithiation described by $x_{\text{average}} = 1$. (d) and (e) are the counterparts of (b) and (c) during the delithiation half cycle, respectively.

opposite to the trend during the lithiation half cycle. It is interesting to note that the associated mean stress distribution is reversed with the transition from lithiation to delithiation: those regions initially under tensile mean stress are now mainly under compression and *vice versa*. This trend is clearly shown in Fig. 5d and e. The regions labelled by a through k are geometrically complementary to those hydrostatically tensile regions denoted by A through G in Fig. 5b and c. Therefore, nearly all of the nanowalls experience a significant tensile mean stress at a certain stage during a lithiation/delithiation cycle. As a result, pores are likely to form throughout the entire nanowalls after many cycles. This prediction is confirmed by the experimentally observed homogeneous pore distribution in the nanowall structures observed in experiments (Fig. 4).

The simulation results of significant tensile mean stress in the nanowalls can be used to derive the critical void size R_c for pore formation. For simplicity, we assume that the surface energy γ of lithiated silicon is independent of lithium concentration with a value of 1 J m^{-2} .²¹ The values of R_c corresponding to the region under tensile stress during lithiation and delithiation are summarized in Table S1(a) and (b),[†] respectively. The critical radii in all regions range from 2–13.3 nm. Such an estimate agrees with experimental observation: the radii of the pores in the nanowalls after 40 lithiation/delithiation cycles are much greater than 13.3 nm (Fig. 4c), indicating that voids greater than the critical size grow into larger pores under significant tensile mean stress.

Conclusion

In summary, we designed a novel 2-D a-Si nanowall structure as an anode for Li ion batteries that exhibits excellent electrochemical properties. The lower specific surface area of the nanowall structure compared to 1-D/0-D nanostructures leads to a relatively high first CE. A high specific capacity of $\sim 2100 \text{ mA h g}^{-1}$ is obtained at C/5 and remains stable for over 40 cycles. Porous structures form throughout the nanowalls after cycles, which is attributed to the complementary distributions of the

tensile mean stress in the nanowalls induced by lithiation and delithiation. The cycling performance of proof-of-concept devices can be further improved with improving the uniformity and bonding between the Si nanowalls and the substrate. It is anticipated based on the mechanical modelling that the nanowall anodes can be excellent candidates for flexible energy devices. Such nanostructures can potentially lead to many other applications including solar, water splitting and others, where both a nanoscale structure to manipulate electrons and photons and a low surface area to avoid side reaction and recombination are needed.

Acknowledgements

Jiayu Wan, Alex Kaplan and Zheng Jia contributed to this work equally. L. Hu acknowledges the financial start up support from the University of Maryland. A. F. Kaplan and L. J. Guo acknowledge support by NSF grant CMII #1000425. Z. Jia and T. Li acknowledge support by NSF grants CMMI #0928278 and #1069076. We would like to thank Professor Chunsheng Wang for sharing the glove box and battery accessories and Professor Peter Kofinas for sharing the Sartorius Microbalance. We acknowledge the support of the Maryland Nanocenter, its Fablab and its Nisplab. The Nisplab is supported in part by the NSF as a MRSEC shared experimental facility.

Notes and references

- 1 M. Armand and J. M. Tarascon, *Nature*, 2008, **451**, 652–657.
- 2 B. Kang and G. Ceder, *Nature*, 2009, **458**, 190–193.
- 3 I. Kovalenko, B. Zdyrko, A. Magasinski, B. Hertzberg, Z. Milicev, R. Burtovyy, I. Luzinov and G. Yushin, *Science*, 2011, **334**, 75–79.
- 4 X. Ji, K. T. Lee and L. F. Nazar, *Nat. Mater.*, 2009, **8**, 500–506.
- 5 J. B. Goodenough and Y. Kim, *Chem. Mater.*, 2009, **22**, 587–603.
- 6 M. Whittingham, *MRS Bull.*, 2008, **33**, 411–419.
- 7 C. K. Chan, H. Peng, G. Liu, K. McIlwrath, X. F. Zhang, R. A. Huggins and Y. Cui, *Nat. Nanotechnol.*, 2008, **3**, 31–35.

- 8 A. Magasinski, P. Dixon, B. Hertzberg, A. Kvit, J. Ayala and G. Yushin, *Nat. Mater.*, 2010, **9**, 353–358.
- 9 H. Kim and J. Cho, *Nano Lett.*, 2008, **8**, 3688–3691.
- 10 H. K. Liu, Z. P. Guo, J. Z. Wang and K. Konstantinov, *J. Mater. Chem.*, 2010, **20**, 10055–10057.
- 11 T. H. Hwang, Y. M. Lee, B.-S. Kong, J.-S. Seo and J. W. Choi, *Nano Lett.*, 2011, **12**, 802–807.
- 12 Y.-S. Hu, R. Demir-Cakan, M.-M. Titirici, J.-O. Mueller, R. Schloegl, M. Antonietti and J. Maier, *Angew. Chem., Int. Ed.*, 2008, **47**, 1645–1649.
- 13 X. Zhou, L.-J. Wan and Y.-G. Guo, *Small*, 2013, **9**, 2684–2688.
- 14 M.-H. Park, M. G. Kim, J. Joo, K. Kim, J. Kim, S. Ahn, Y. Cui and J. Cho, *Nano Lett.*, 2009, **9**, 3844–3847.
- 15 J. Xie, X. Yang, S. Zhou and D. Wang, *ACS Nano*, 2011, **5**, 9225–9231.
- 16 H. T. Nguyen, F. Yao, M. R. Zamfir, C. Biswas, K. P. So, Y. H. Lee, S. M. Kim, S. N. Cha, J. M. Kim and D. Pribat, *Adv. Energy Mater.*, 2011, **1**, 1154–1161.
- 17 H. Kim, B. Han, J. Choo and J. Cho, *Angew. Chem.*, 2008, **120**, 10305–10308.
- 18 T. D. Hatchard and J. R. Dahn, *J. Electrochem. Soc.*, 2004, **151**, A838–A842.
- 19 C.-M. Wang, X. Li, Z. Wang, W. Xu, J. Liu, F. Gao, L. Kovarik, J.-G. Zhang, J. Howe, D. J. Burton, Z. Liu, X. Xiao, S. Thevuthasan and D. R. Baer, *Nano Lett.*, 2012, **12**, 1624–1632.
- 20 X. H. Liu, H. Zheng, L. Zhong, S. Huang, K. Karki, L. Q. Zhang, Y. Liu, A. Kushima, W. T. Liang, J. W. Wang, J.-H. Cho, E. Epstein, S. A. Dayeh, S. T. Picraux, T. Zhu, J. Li, J. P. Sullivan, J. Cumings, C. Wang, S. X. Mao, Z. Z. Ye, S. Zhang and J. Y. Huang, *Nano Lett.*, 2011, **11**, 3312–3318.
- 21 I. Ryu, J. W. Choi, Y. Cui and W. D. Nix, *J. Mech. Phys. Solids*, 2011, **59**, 1717–1730.
- 22 H. Yang, S. Huang, X. Huang, F. Fan, W. Liang, X. H. Liu, L.-Q. Chen, J. Y. Huang, J. Li, T. Zhu and S. Zhang, *Nano Lett.*, 2012, **12**, 1953–1958.
- 23 F.-F. Cao, J.-W. Deng, S. Xin, H.-X. Ji, O. G. Schmidt, L.-J. Wan and Y.-G. Guo, *Adv. Mater.*, 2011, **23**, 4415–4420.
- 24 Y. He, B. Yang, K. Yang, C. Brown, R. Ramasamy, H. Wang, C. Lundgren and Y. Zhao, *J. Mater. Chem.*, 2012, **22**, 8294–8303.
- 25 B. Varghese, M. V. Reddy, Z. Yanwu, C. S. Lit, T. C. Hoong, G. V. Subba Rao, B. V. R. Chowdari, A. T. S. Wee, C. T. Lim and C.-H. Sow, *Chem. Mater.*, 2008, **20**, 3360–3367.
- 26 H. R. Byon, B. M. Gallant, S. W. Lee and Y. Shao-Horn, *Adv. Funct. Mater.*, 2013, **23**, 1037–1045.
- 27 E. Yoo, J. Kim, E. Hosono, H.-s. Zhou, T. Kudo and I. Honma, *Nano Lett.*, 2008, **8**, 2277–2282.
- 28 C. H. Xu, B. H. Xu, Y. Gu, Z. G. Xiong, J. Sun and X. S. Zhao, *Energy Environ. Sci.*, 2013, **6**, 1388–1414.
- 29 S. Kurita, A. Yoshimura, H. Kawamoto, T. Uchida, K. Kojima, M. Tachibana, P. Molina-Morales and H. Nakai, *J. Appl. Phys.*, 2005, **97**, 104320.
- 30 S. H. Ahn and L. J. Guo, *Adv. Mater.*, 2008, **20**, 2044–2049.
- 31 V. L. Pushparaj, M. M. Shaijumon, A. Kumar, S. Murugesan, L. Ci, R. Vajtai, R. J. Linhardt, O. Nalamasu and P. M. Ajayan, *Proc. Natl. Acad. Sci. U. S. A.*, 2007, **104**, 13574–13577.
- 32 K.-H. Choi, S.-H. Kim, H.-J. Ha, E.-H. Kil, C. K. Lee, S. B. Lee, J. K. Shim and S.-Y. Lee, *J. Mater. Chem. A*, 2013, **1**, 5224–5231.
- 33 L. J. Guo, *Adv. Mater.*, 2007, **19**, 495–513.
- 34 J. Wang, Z. Li, N. Singh and S. Lee, *Opt. Express*, 2011, **19**, 23078–23084.
- 35 M. M. Brewster, M.-Y. Lu, S. K. Lim, M. J. Smith, X. Zhou and S. Gradečak, *J. Phys. Chem. Lett.*, 2011, **2**, 1940–1945.
- 36 P. H. L. Notten, F. Roozeboom, R. A. H. Niessen and L. Baggetto, *Adv. Mater.*, 2007, **19**, 4564–4567.
- 37 C. Trompoukis, O. El Daif, V. Depauw, I. Gordon and J. Poortmans, *Appl. Phys. Lett.*, 2012, **101**, 103901–103904.
- 38 A. F. Kaplan, T. Xu and L. J. Guo, *Appl. Phys. Lett.*, 2011, **99**, 143111–143113.
- 39 M.-G. Kang, H. Joon Park, S. Hyun Ahn and L. Jay Guo, *Sol. Energy Mater. Sol. Cells*, 2010, **94**, 1179–1184.
- 40 Y. Yang, K. Mielczarek, M. Aryal, A. Zakhidov and W. Hu, *ACS Nano*, 2012, **6**, 2877–2892.
- 41 T. Ling, S.-L. Chen and L. J. Guo, *Opt. Express*, 2011, **19**, 861–869.
- 42 P. Mukherjee, A. Bruccoleri, R. K. Heilmann, M. L. Schattenburg, A. F. Kaplan and L. J. Guo, *J. Vac. Sci. Technol. B*, 2010, **28**, C6P70.
- 43 Y. Yao, N. Liu, M. T. McDowell, M. Pasta and Y. Cui, *Energy Environ. Sci.*, 2012, **5**, 7927–7930.
- 44 R. Demir Cakan, M.-M. Titirici, M. Antonietti, G. Cui, J. Maier and Y.-S. Hu, *Chem. Commun.*, 2008, 3759–3761.
- 45 Y. He, X. Yu, Y. Wang, H. Li and X. Huang, *Adv. Mater.*, 2011, **23**, 4938–4941.
- 46 K. Zhao, M. Pharr, Q. Wan, W. L. Wang, E. Kaxiras, J. J. Vlassak and Z. Suo, *J. Electrochem. Soc.*, 2012, **159**, A238–A243.

Supporting Information

Two Dimensional Silicon Nanowalls for Lithium Ion Batteries

Jiayu Wan,^{1,(a)} Alex F. Kaplan,^{2,(a)} Jia Zheng,^{3,(a)} Xiaogang Han,¹ Yuchen Chen,¹ Nicholas J. Waddock,¹ Nicholas Faenza,¹ Teng Li,^{3,*} Jay Guo,^{2,*} and Liangbing Hu,^{1,*}

¹*Department of Materials Science and Engineering, University of Maryland, College Park, MD, USA, 20742*

**Email: Binghu@umd.edu*

²*Department of Electrical Engineering and Computer Science, University of Michigan, Ann Arbor, MI, USA, 48109*

**Email: Guo@umich.edu*

³*Department of Mechanical Engineering, University of Maryland, College Park, MD, USA, 20742*

**Email: LiT@umd.edu*

(a) These authors contribute equally to this work

1. Modeling details

To gain insights on the nano-pore formation and stress generation during lithiation and delithiation, we have simulated the concurrent diffusion and mechanical deformation during initial lithiation and following delithiation of the amorphous silicon nanowall using finite

element package ABAQUS 6.10. The diffusion and elastic-perfectly plastic model is employed and the material undergoes elastic and/or plastic deformation where the von Mises yield criterion determines plastic yielding. The plastic deformation is governed by the J2-flow rule. The normalized lithium concentration and stress-strain fields are numerically solved by a fully-coupled implicit temperature-displacement procedure in ABAQUS/Standard, given that governing equations of diffusion is essentially equivalent to those of heat. During simulation the normalized lithium concentration and associated stress-strain deformation are updated incrementally. The normalized lithium concentration is defined as the current concentration (i.e. x in Li_xSi) divided by the concentration at fully-lithiated stage ($x = 4.2$) and it is equivalent to the “temperature” in above-mentioned numerical procedure. The lithiation-induced volumetric strain is equivalently to the “thermal strain” caused by “temperature” change. The coefficient of thermal expansion is chosen to be 0.6 and thus the accordingly volumetric expansion is 400% when the “temperature” in simulation (i.e. normalized lithium concentration) reaches 1.

The dimension of the nanowall is 600nm×900nm×50nm. Taking advantage of symmetry, only $\frac{1}{4}$ of the nanowall is simulated in order to reduce the numerical expense, with symmetry boundary condition is employed at mid-planes $z = 0$ and $x = 0$. The Young’s modulus and Poisson’s ratio of lithiated silicon are both assumed to vary linearly with Li concentration from 160 to 40 GPa and from 0.24 to 0.22 respectively ^[1,2]. The yielding stress of lithiated silicon is chosen to be 2GPa. Diffusivity of lithium in silicon is assumed to be a constant of 10^{-13} cm²/s ^[3]. The amorphous silicon nano-wall is initially pristine and subjected to a constant C/5 charging/discharging rate at the outer surface. In the simulation, the lithiation half cycle is terminated when $x_{average}$ reaches 2 and delithiation half cycle begins with the final lithium concentration and stress-strain field at the end of lithiation half cycle. The displacements at the

bottom surface of nanowall are all fixed to zero and all other outer surfaces are traction free.

2. Additional simulation results

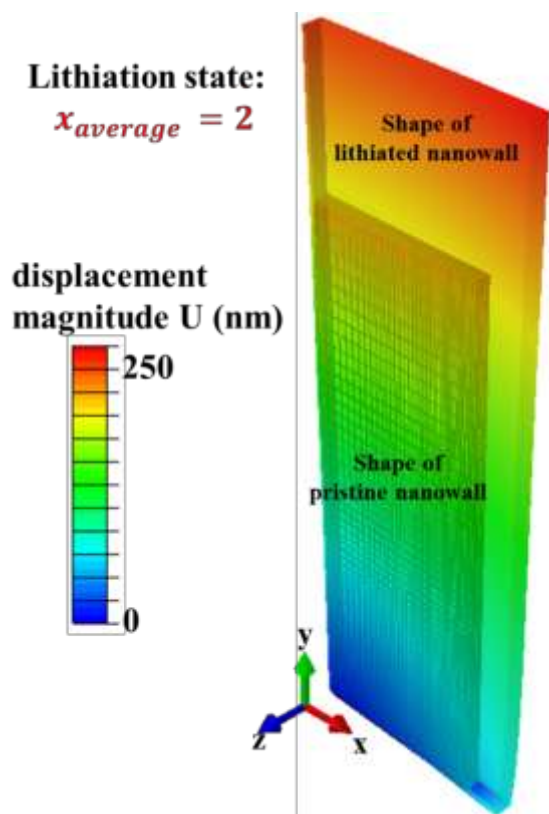


Figure S1 Volume expansion before (pristine nanowall) and after lithiation half cycle ($x_{average} = 2$). $x_{average}$ reaches 2 at the end of the lithiation cycle, resulting in a ~200% volume expansion of the nanowall. Mesh of the pristine nanowall is also shown (Note: the triad is only used to show the directions of coordinate but it does NOT represent the real coordinate system of which the origin is at the center of the bottom surface. Same for **Figure S2**, **S3** and **S4**).

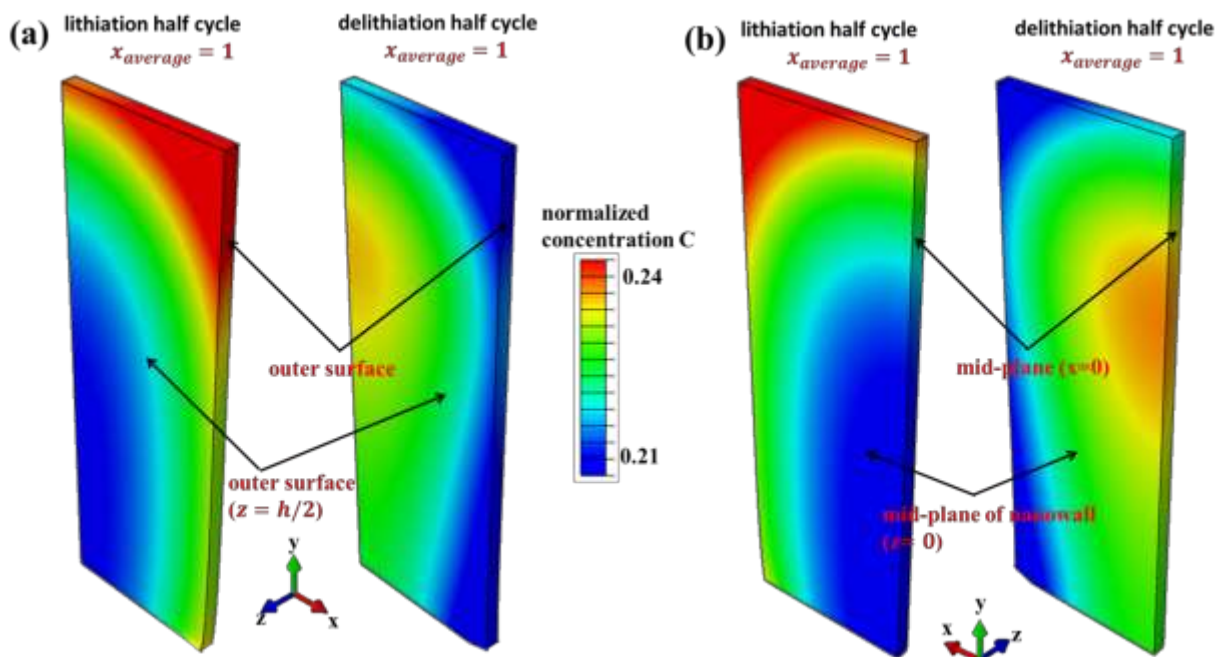


Figure S2. (a). Normalized Li concentration distribution at the outer surface during lithiation half cycle (left) and delithiation half cycle (right) when $x_{average} = 1$, from a perspective view. Concentration profile at the outer surface on the side of nanowall is also available from this perspective. Rotating the perspective view in (a) by 180° with respect to y axis gives (b) the perspective view of the similar plots at mid-planes ($x = 0$ and $z = 0$). During lithiation, concentration is higher near the outer surface but lower in the interior of nanowall; during delithiation, concentration is higher in the interior of nanowall but lower near the outer surface.

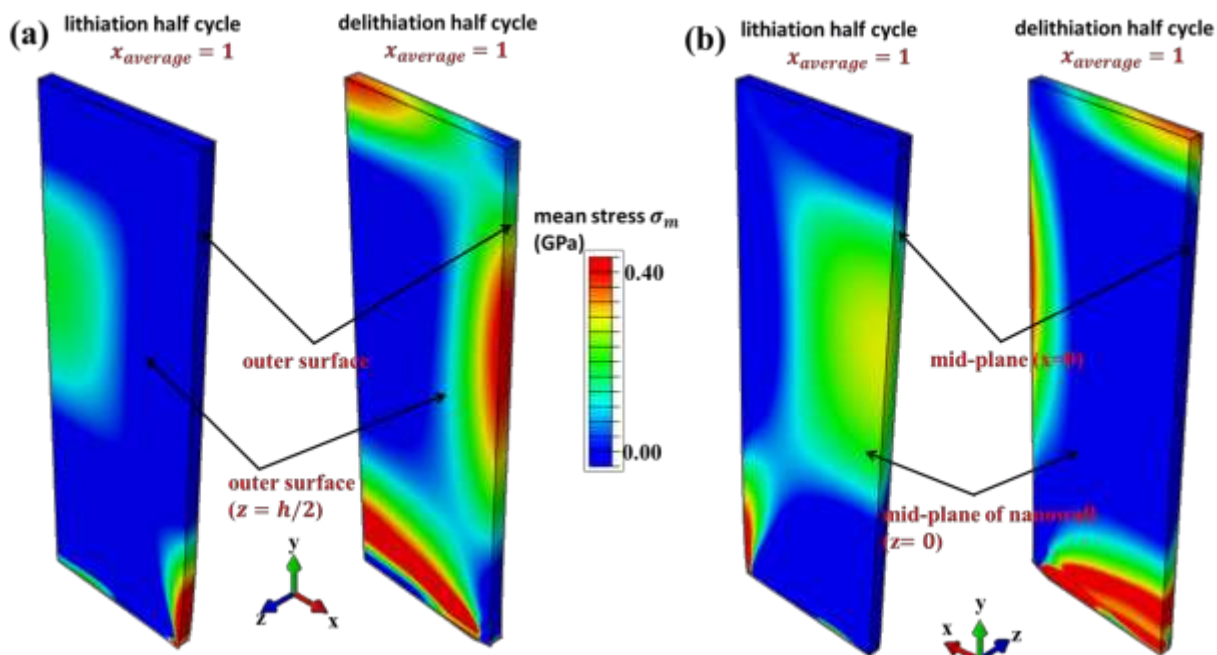


Figure S3. (a) Distribution of mean stress σ_m at the outer surface of the nanowall during lithiation half cycle (left) and delithiation half cycle (right) when $x_{average} = 1$ from a perspective view. (b). The perspective view of the similar plots at the mid-planes ($x = 0$ and $z = 0$).

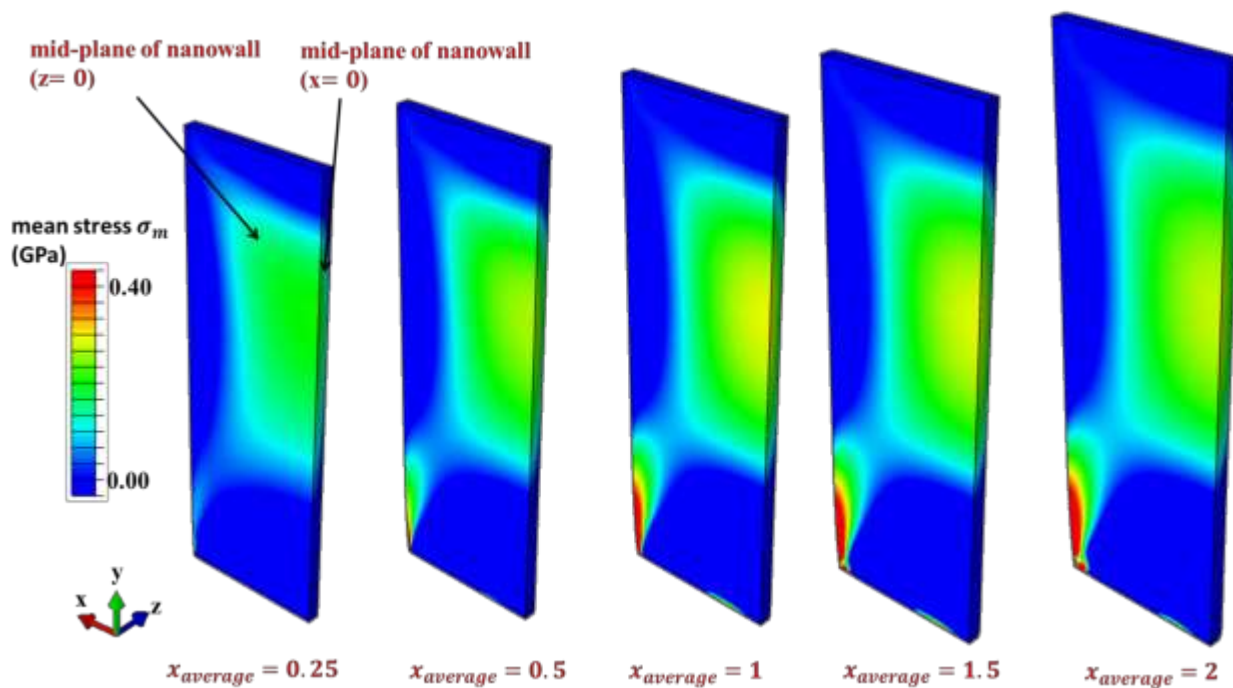


Figure S4. Mean stress σ_m evolution during lithiation half cycle. Note that the mean stress level in the nanowall increases with the extent of lithiation and nearly saturates after $x_{average}$ exceeds 1.

Table S1 (a) Mean stress range and critical radii R_c in highlighted regions in Figure 5 b, c (at lithiation half cycle with $x_{average} = 1$)

Region	A	B	C,F	D,G	E
mean stress range (GPa)	0.25~0.28	0.15~0.25	0.15~0.30	0.30~0.60	0.15~0.18
critical radius R_c (nm)	7.1~8	8~13.3	6.67~13.3	3.33~6.67	11.1~13.3

Table S1 (b) mean stress range and critical radii R_c in highlighted regions in Figure 5d, e (at delithiation half cycle with $x_{average} = 1$)

Region	a	b,c,e,g,h,k	d,i	f,j
mean stress range (GPa)	0.35~0.4	0.15~0.35	0.35~1	0.35~0.4
critical radius R_c (nm)	5~5.71	5.71~13.3	2~5.71	5~5.71

3. Materials details

The Si thin film is prepared by e-beam deposition under 4×10^{-7} torr. The deposition chamber is pumped down overnight to achieve the a low vacuum level, in order to get high purity Si. EDS data of Si thin film on stainless steel substrate shows a high purity of 96.33wt% of Si with impurities of C, O, Al of 1.38wt%, 1.20wt%, 1.09wt%, respectively. The Al impurity may be a residual impurity from the e-beam evaporator crucible. C and O may come from the substrate and surface oxidation of the thin film.

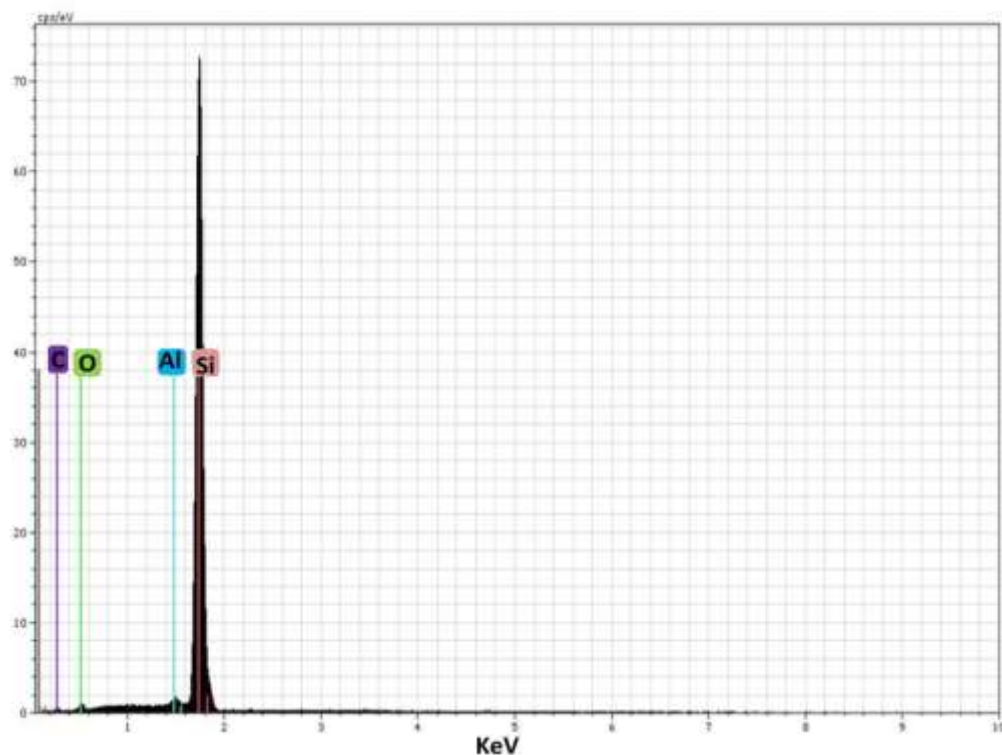


Figure S5. EDS results of prepared e-beam deposited a-Si thin film

Table S2. Si thin film composition by EDS

El	An	Series	Concentration(wt%)	C atom(at. -%)	Err (%)
C	6	K-series	1.38	3.13	0.4
O	8	K-series	1.20	2.05	0.3
Al	13	K-series	1.09	1.10	0.1
Si	14	K-series	96.33	93.72	4.5

Figure S6 shows the EDS mapping (top view) of the nanowall structure, all from the same area. From **Figure S6a** and **S6c** we can clearly see the nanoimprint nanowall arrays. However **Figure S6b** shows the whole area is covered by Cr (Cr mask and binding enhancing layer). This proves there are residual Cr mask on top of Si nanowall.

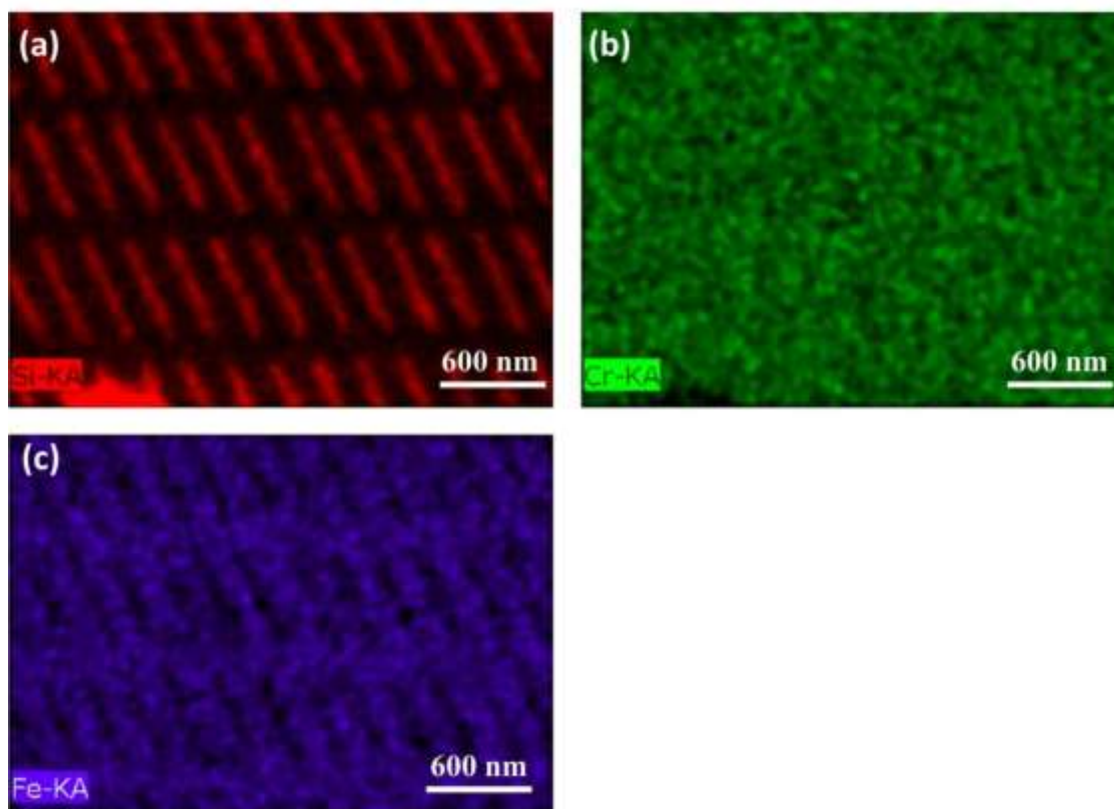


Figure S6. EDS mapping result of Si nanowall structure before cycling, in the same area (a) Si mapping; (b). Cr mapping; (c). Fe mapping

References and Notes

1. Zhao, K.; Pharr, M.; Wan, Q.; Wang, W. L.; Kaxiras, E.; Vlassak, J. J.; Suo, Z., Concurrent Reaction and Plasticity during Initial Lithiation of Crystalline Silicon in Lithium-Ion Batteries. *Journal of The Electrochemical Society* 2012, 159, A238-A243.
2. Obrovac, M. N.; Christensen, L.; Le, D. B.; Dahn, J. R., Alloy Design for Lithium-Ion Battery Anodes. *Journal of The Electrochemical Society* 2007, 154, A849-A855.
3. Haftbaradaran, H.; Gao, H.; Curtin, W. A., A surface locking instability for atomic intercalation into a solid electrode. *Applied Physics Letters* 2010, 96, 091909-3.